Enhanced interfacial charge migration through fabrication of p-n junction in $ZnIn_2S_4/NiFe_2O_4$/biochar composite for photocatalytic doxycycline hydrochloride degradation

Qiong Wu [a], Youtao Song [a,b,*]

[a] *School of Environmental Science, Liaoning University, Shenyang, China*
[b] *International Engineering Technology Research Institute of Urban and Energy Environment, Liaoning University, Shenyang, China*

ABSTRACT

Photo-induced electron-hole pair recombination, light response ability and surface property of photocatalyst greatly affect its activity. In this paper, a p-n junction $ZnIn_2S_4/NiFe_2O_4$ with biochar (ZIS/NFO/BC) was prepared, presenting improved charge carrier mobility, excellent light absorption and hierarchical porous microstructure. ZIS/NFO/BC exhibited good photodegradation efficiency and TOC removal rate towards doxycycline hydrochloride under simulated sunlight, as well as good stability and reusability after six cycles. Biochar inhibited the agglomeration of nanoparticles, improved charge carrier mobility and light absorption ability. The synergy between adsorption of biochar and photocatalytic degradation of p-n junction greatly promoted photodegradation efficiency. Photo-induced holes (h^+) played a major role during photodegradation. The effects of pH, coexisting ions (Cl^-, NO_3^-, CO_3^{2-}) and humic acid on photodegradation were investigated. Furthermore, the photodegradation mechanism was proposed and possible pathway was illustrated. This work provides new route for the development of magnetic recyclable photocatalyst with high potential for wastewater treatment.

1. Introduction

Nowadays, large amounts of industrial and agricultural effluents are generated every day, which may contain refractory organic pollutants like dyes, antibiotics, phenols, polycyclic aromatic hydrocarbons (PAHs), etc. These toxic compounds can cause great harm to both public health and ecosystem. However, conventional water treatment techniques (for instance, adsorption, membrane filtration, and chemical-based degradation) cannot completely degrade persistent pollutants, presenting various disadvantages. Adsorption and filtration methods can't degrade pollutants, only transferring them from wastewater to other places, and this may cause secondary pollution. Chemical-based treatment often results in the formation of sludge, which also becomes a threat to water quality. The requirement of looking for an efficient, low cost and green wastewater treatment process is becoming very urgent. As a promising wastewater treatment method, advanced oxidation processes (AOPs) has been intensively focused by scientists [1]. AOP is the process that produces reactive oxygen species to degrade organic molecules in wastewater [2]. Many AOPs techniques have been reported, such as photocatalysis, ultrasonic degradation, microwave-

assisted degradation, electrochemical process, Fenton and Fenton-like processes [3]. The utilization of AOP can achieve high degradation performance towards refractory organic pollutants [4]. However, there are several disadvantages about various AOPs. As for Fenton process, sludge was formed due to the usage of Fe-based chemical and H_2O_2 reagent. The elimination of sludge inevitably increases operation costs [5]. As for ultrasonic degradation, its high costs are ascribed to the electricity consumption [6]. Compared with the above-mentioned AOP processes, the advantages of photocatalysis are: no consumption of electrical or fossil energy, no requirement of additional chemical reagents [7].

Semiconductor-based sunlight-driven photocatalysis has become an important research topic recently, due to its wide application such as photocatalytic nitrogen fixation [8], water splitting and hydrogen production [9], degradation of refractory aqueous pollutants [10]. In recent years, a wide range of photocatalysts have been reported, such as metal oxide [11], sulfides [12], and phosphides [13]. One typical sulfide semiconductor, $ZnIn_2S_4$, with good sunlight response, has been reported to exhibit excellent performance in many photocatalytic fields [14–16]. Researchers have been focusing on methods to improve its practical

application potential in two aspects, one is to promote photo-induced charge carrier transportation (equal to the inhibition of charge carrier recombination), the other is to increase its stability and recyclability for long-term performance.

Coupling with another cocatalyst is reported as an excellent solution for both aspects. Yang et al. reported the electrostatic self-assembled $ZnIn_2S_4$/protonated g-C_3N_4 heterojunction with good hydrogen production [17]. They attributed this to the appropriate energy bands of both components, which effectively promoted charge carrier movement at the interface [17]. This promoted mobility also hinders photocorrosion of $ZnIn_2S_4$ [17], and similar report also confirmed this viewpoint [18]. Among various cocatalysts, p-type semiconductor $NiFe_2O_4$ has attracted huge attention due to the construction of p-n junction with *n*-type semiconductor. Fu et al. [19] immobilized $NiFe_2O_4$/MoS_2 p-n junction onto Pd, which exhibited enhanced photocatalytic activity due to the superior charge carrier transfer. Pd particles further suppressed charge carrier recombination. Similar improvements of substrate immobilization have also been reported, for instance, Yuan et al. [20] immobilized MoS_2/$ZnIn_2S_4$ heterojunction onto graphene, which showed efficient solar hydrogen generation due to the electron conductivity of graphene. However, both noble metal Pd and graphene are very expensive, and their fabrication processes are very sophisticated. In recent years, alternatives to replace these substrates have been proposed [21], and one typical material is biochar [22]. Like the above-mentioned substrates, biochar also exhibits good electric conductivity, which is beneficial to photo-induced electron transfer and thus hinders charge carrier recombination. Zhou et al. also mentioned that the porous structure of biochar improved the adsorption ability of photocatalytic composite, which also facilitated the photodegradation process [23].

Inspired by the above-mentioned state-of-the-art review, in this work, we immobilized $NiFe_2O_4$ (NFO) nanoparticles onto biochar (BC) by hydrothermal method. And then $ZnIn_2S_4$ (ZIS) nanoparticles were introduced by solvothermal method to produce ternary ZIS/NFO/BC composite. The widely used antibiotic doxycycline hydrochloride (DOXH) was chosen as target pollutant to evaluate the photodegradation efficiency of reported catalyst and related control samples under simulated sunlight (Ultraviolet–Visible light, abbreviated as UV–vis). After conducting a series of relevant characterization tests, we combined the results with degradation data to further study the photodegradation intermediates and mechanism. The effects of environmental factors on photodegradation efficiency were studied, including initial pH of DOXH solution, coexisting anions and humic acid. Due to the magnetism of NFO component and charge carrier mobility, ZIS/NFO/BC exhibited good reusability and stability, which signified its great potential to be applied in environmental pollutant control applications.

Although plenty of papers have been published on $ZnIn_2S_4$-based heterojunction and its photocatalytic applications, very few of them reported the immobilization onto substrates. In this work, $ZnIn_2S_4$/$NiFe_2O_4$ (ZIS/NFO) p-n junction was immobilized onto biochar to form ZIS/NFO/BC photocatalytic composite. Biochar inhibited the agglomeration of photocatalytic nanoparticles, which resulted in the improvement of surface condition and photocatalytic performance. Due to the conductivity function, biochar prevented the photo-corrosion of $ZnIn_2S_4$ by improving the mobility and separation of photo-induced electron-hole pairs, ensuring good stability and reusability of ZIS/NFO/BC. Compared with ZIS/NFO, ZIS/NFO/BC not only presented higher photocatalytic degradation performance, but also reduced the content ratios of both ZIS and NFO. This greatly lowered the potential risk of metal leaching.

2. Experimental

2.1. Preparation

All the involved chemical reagents are listed in Table S1 (Supplementary Information), and were used without further purification.

Biochar was prepared by a typical pyrolysis procedure. Crushed corn straw was put in a crucible and then pyrolyzed in an oxygen-limited muffle furnace at 450 ℃ for 2 h. The heating rate was set at 3 ℃/min. The obtained biochar was washed by deionized water and dried at 80 ℃.

A series of $NiFe_2O_4$/biochar with varied mass ratio (denoted as NFO/BC-*x*, *x* = 1, 2, 3 or 4) were fabricated by hydrothermal procedure. In a typical preparation process of NFO/BC-1, The Ni precursor (Ni $(NO_3)_2$·6H$_2$O, 0.05 g) and Fe precursor (Fe(NO$_3$)$_3$·9H$_2$O, 0.14 g) were mixed with citric acid (0.10 g) and biochar (2.0 g), and put in deionized water (50 mL) under constant stirring. The mixture was then sonicated for 30 min and changed back to constant stirring for 1 h. After that, the mixture was transferred into a Teflon-lined autoclave and heated at 160 ℃ for 20 h. The black powder in the autoclave was collected and washed by deionized water for three times, and then heated at 90 ℃ overnight. Similar processes were carried out to obtain NFO/BC-*x* (*x* = 2, 3, 4), except that the amount of Ni precursor, Fe precursor and citric acid was multiplied by *x*. Pure $NiFe_2O_4$ was also fabricated via this procedure without the addition of biochar.

A series of $ZnIn_2S_4$/$NiFe_2O_4$/biochar (denoted as ZIS/NFO/BC-*x*, *x* = 1, 2, 3 or 4) were fabricated by solvothermal procedure. In a typical fabrication of ZIS/NFO/BC-1, the Zn precursor (Zn(NO$_3$)$_2$·6H$_2$O, 0.60 g), the In precursor (In(NO$_3$)$_3$·4.5H$_2$O, 1.50 g) and thioacetamide (0.60 g) were mixed with glycerol (20 mL) and N,*N*-Dimethylformamide (50 mL), under constant stirring. After sonicated for 1 h, NFO/BC-1 was added into the mixture, which was then sonicated for another 1 h. The resultant mixture was put in a Teflon-lined autoclave and heated at 180 ℃ for 10 h. After that, the obtained product was filtered and then washed several times by deionized water. The final product was then dried at 55 ℃. ZIS/NFO/BC-*x* (*x* = 2, 3 or 4) was also fabricated via the same route, except that NFO/BC-1 was replaced by NFO/BC-2, NFO/BC-3 or NFO/BC-4, respectively. Similar preparation procedures were carried out to obtain ZIS/BC or pure ZIS, and the only difference is the replacement of NFO/BC by biochar, or no addition, respectively. ZIS/NFO was fabricated via the similar route of ZIS/NFO/BC-3, and during this procedure, NFO/BC-3 was replaced by NFO, while the mass ratio of ZIS and NFO was kept the same to that in ZIS/NFO/BC-3.

2.2. Characterization

All technologies utilized for characterization, such as XRD, FTIR, XPS, SEM, TEM, are provided in Table S2.

2.3. Photodegradation efficiency evaluation

The photodegradation efficiencies of all samples were investigated by degradation of DOXH under simulated sunlight irradiation (Xe light bulb, 150 W, TENLIN Light Instrument Co., ltd). The intensity on the surface of DOXH solution was measured as 9.0 mW/cm^2. Typically, varied amount of catalyst sample was added into 50 mL of DOXH solution (30 mg/L) to build reaction system, with constant stirring. The system was kept under dark for 30 min to achieve adsorption–desorption equilibrium which has been verified in Fig. S1. After that, the system was irradiated by Xe light bulb, and its temperature was kept at ambient condition via a cooling jacket between light source and the system. At varied time interval, the aliquot of 3.5 mL was taken out from the system and centrifuged to obtain the supernatant, the concentration of which was measured via a UV–vis Spectrophotometer (Table S2) at 274 nm. The concentration change at different time periods can be reflected by the corresponding concentration ratio C/C_0, in which C and C_0 represent the concentration of DOXH solution after treated and its initial concentration, respectively. Every single test was carried out in three times, and the ratio value in the figure is the average of these parallel test results.

The effect of initial pH of DOXH solution on photodegradation efficiency was studied. The pH value was tuned by adding HCl solution (1.0 M) or NaOH solution (0.1 M), and monitored by a pH meter (Table S2).

The effects of coexisting anions (Cl$^-$, NO$_3^-$ or CO$_3^{2-}$) or humic acid (HA) with different concentrations were also evaluated (Table S1).

To evaluate the recyclability of ZIS/NFO/BC-3, the reusing tests were carried out: after the first round of degradation, the sample was separated and then washed several times by deionized water, then dried at 55 °C overnight. The resultant powder was used for the next round of photodegradation.

Scavenging tests were carried out to detect reactive oxidation species (ROS) during DOXH photodegradation. The scavenger IPA (Isopropanol, 1.0 mM), EDTA-2Na (Ethylenediaminetetraacetic acid disodium salt, 1.0 mM) or BQ (Benzoquinone, 1.0 mM) was added into the system before photodegradation test, in order to quench ·OH, h$^+$ or ·O$_2^-$, respectively.

The intermediates formed during DOXH photodegradation were evaluated by HPLC-MS technique (Table S2).

3. Results and discussion

3.1. XRD analysis

The crystal phase and crystallographic structure of selected samples were studied by XRD method. As presented in Fig. 1a, the typical peaks of biochar between 25.0° and 30.0° can be attributed to its impurity SiO$_2$ (ref). As for pure ZIS, the diffraction peaks at 27.7°, 30.7° and 47.2° correspond to the (1 0 2), (1 0 4) and (1 1 0) crystal planes of hexagonal phase ZIS (JCPDS. No. 65–2023) [24]. The diffraction peaks of pure NFO at 30.3°, 35.7°, 43.4°, 53.9°, 57.1° and 62.9° can be designated to the (2 2 0), (3 1 1), (4 0 0), (4 2 2), (5 1 1) and (4 4 0) crystal planes of spinel structure (JCPDS. No. 10–0325), respectively [25]. The XRD patterns of ZIS/NFO and ZIS/NFO/BC-3 are similar to that of pristine ZIS, which implies that the introduction of tiny amount of NFO did not restrict the formation of ZIS.

3.2. FTIR spectra

The FTIR spectra of biochar, ZIS, NFO, ZIS/NFO and ZIS/NFO/BC-3 are illustrated in Fig. 1b. The FTIR spectrum of NFO shows two peaks at 590 cm^{-1} and 405 cm^{-1}, which correspond to the metal–oxygen bonds due to Fe$_3$O$_4$ and NiO [26,27]. The peaks at 1382 cm^{-1} and 1034 cm^{-1} are designated to the typical bonds of ZIS [28,29]. The peaks at 1532 cm^{-1}, 1589 cm^{-1} and 1713 cm^{-1} can be attributed to the adsorbed water hydroxyl ions [30]. The broad peak at 3352 cm^{-1} and the weak peak at 3722 cm^{-1} can be ascribed to the O—H stretch, corresponding to the surface hydroxyl groups [31,32]. As for the spectrum of biochar, the wide transmittance waveband from 1000 cm^{-1} to 1400 cm^{-1} corresponds to the C—O stretching and O—H deformation vibration, which are the typical bonds of biochar [33].

3.3. SEM/TEM observation

The morphology of selected samples can be reflected by their SEM images. Fig. 2b shows the typical microsphere morphology of ZIS, which is composed of tiny nanosheets. The morphology of NFO is presented in Fig. 2c, which exhibited an agglomeration phenomenon. Fig. 2a shows the SEM image of biochar, presenting its typical hollow tubules and rough surface. The specific structure provides huge number of loading sites for photocatalytic nanoparticles. The SEM image of ZIS/NFO/BC-3 (Fig. 2d) shows that ZIS microspheres and NFO nanoparticles were evenly dispersed on the surface of biochar, making it a rougher surface. The SEM image with higher magnification (Fig. S2) further indicates that, ZIS nanosheets were immobilized on the surface of biochar, and tiny NFO nanoparticles were evenly dispersed on the surface of both ZIS nanosheets and substrate biochar. Fig. 2e-g shows the EDS spectrum and mappings of ZIS/NFO/BC-3. The spectrum exhibits the peaks of all elements in the sample, and the mapping graphs also prove the existence of these elements: Zn, In, S, Ni, Fe, O and C.

The TEM images (Fig. 3) of ZIS/NFO/BC-3 illustrate its morphology at higher magnification. It can be noticed that ZIS nanosheets and NFO nanoparticles were tightly immobilized onto biochar, leading to a firm heterojunction structure. Furthermore, as presented in Fig. 3c, the lattice fringe spacing of 0.32 nm can be attributed to the (1 1 0) plane of ZIS [24], while the lattice fringe spacing of 0.29 nm can be designated to the (2 2 0) plane of NFO [19]. This further confirms the successful combination of ZIS and NFO.

3.4. XPS analysis

XPS technique was carried out to further analyze the chemical states of ZIS, NFO and ZIS/NFO/BC-3. The survey spectrum of ZIS/NFO/BC-3 (Fig. 4a) shows that all elements, including Zn, In, S, Ni, Fe, O and C were detected. The C 1 s spectrum of ZIS/NFO/BC-3 (Fig. 4b) can be resolved to three peaks at 288.42, 286.53 and 284.80 eV. The first peak corresponds to C=O bond [34]. The second one is designated to metal–carbon bond (Fe-C) and hydroxyl bond (C—O) [35]. The third one is attributed to C—C and C—H bonds from sp^2 hybridized C atom [36].

Fig. 4c-e are the comparisons of Zn 2p, In 3d and S 2p spectra between ZIS and ZIS/NFO/BC-3. For pure ZIS, its Zn 2p spectrum (Fig. 4c) presents the typical peaks at the binding energy (BE) of 1045.20 and 1022.18 eV, which correspond to Zn 2p$_{1/2}$ and Zn 2p$_{3/2}$, respectively [37]. Its In 3d spectrum (Fig. 4d) shows the peaks at 452.71 and 445.18 eV, which are designated to In 3d$_{3/2}$ and Zn In 3d$_{5/2}$, respectively [38]. This implies the existence of In^{3+} [38]. Its S 2p spectrum (Fig. 4e) presents the peaks at 163.20 and 161.94 eV, referring to S 2p$_{1/2}$ and 2p$_{3/2}$, respectively [39]. Compared to ZIS, the peaks in Zn and In spectra of ZIS/NFO/BC-3 shifted to higher BE values. This implies the different chemical environment due to the close combination of ZIS and NFO, in other words, the formation of p-n junction. Once p-n junction was
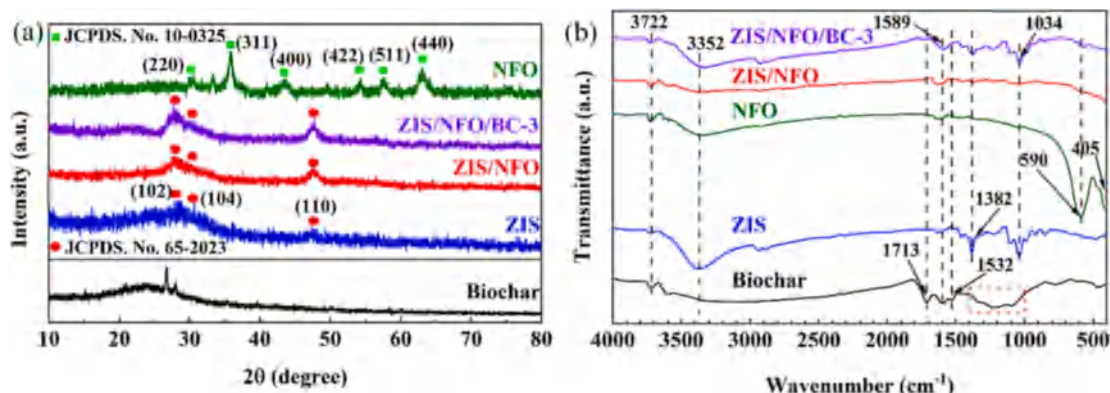

Fig. 1. (a) The XRD patterns and (b) FTIR spectra of biochar, ZIS, NFO, ZIS/NFO, ZIS/NFO/BC-3.
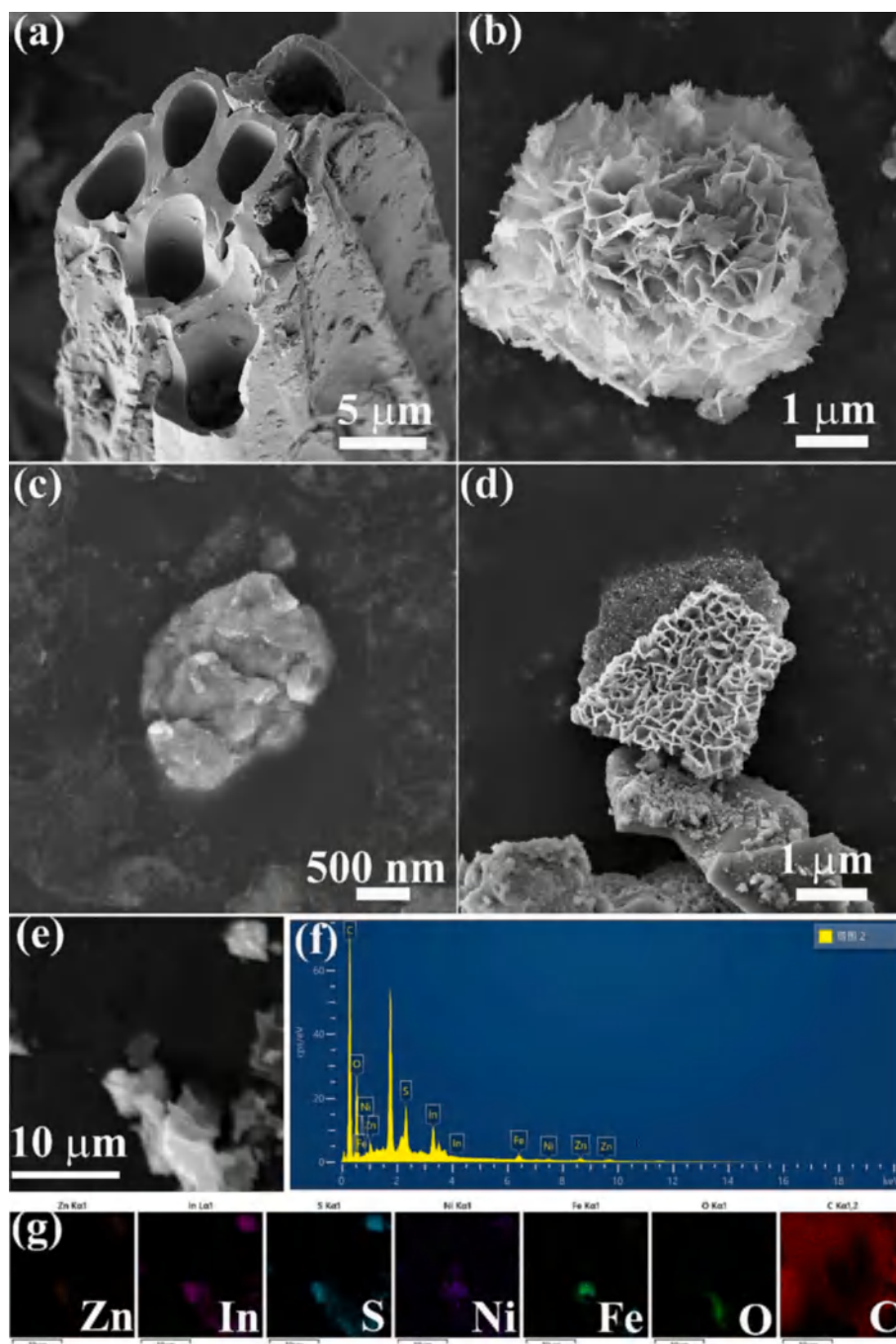
Fig. 2. (a-d) SEM images of biochar, ZIS, NFO and ZIS/NFO/BC-3; (e-g) EDS spectrum and mapping of ZIS/NFO/BC-3.
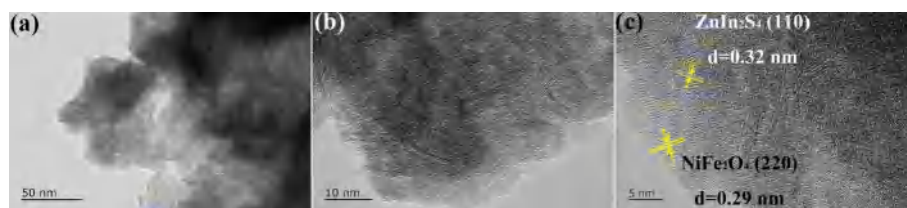

Fig. 3. TEM images of ZIS/NFO/BC-3.

formed, the migration of electrons and holes took place between electron-rich ZIS (*n*-type) and NFO (p-type) [40,41]. Fig. 4f-h is the Ni 2p, Fe 2p and O 1 s spectra of NFO and ZIS/NFO/BC-3. For pristine NFO, its Ni 2p spectrum (Fig. 4f) shows two typical peaks at 872.93 and 854.67 eV, corresponding to Ni 2p$_{1/2}$ and Ni 2p$_{3/2}$, respectively, along with its shake-up satellite peaks [42]. Its Fe 2p spectrum (Fig. 4g)
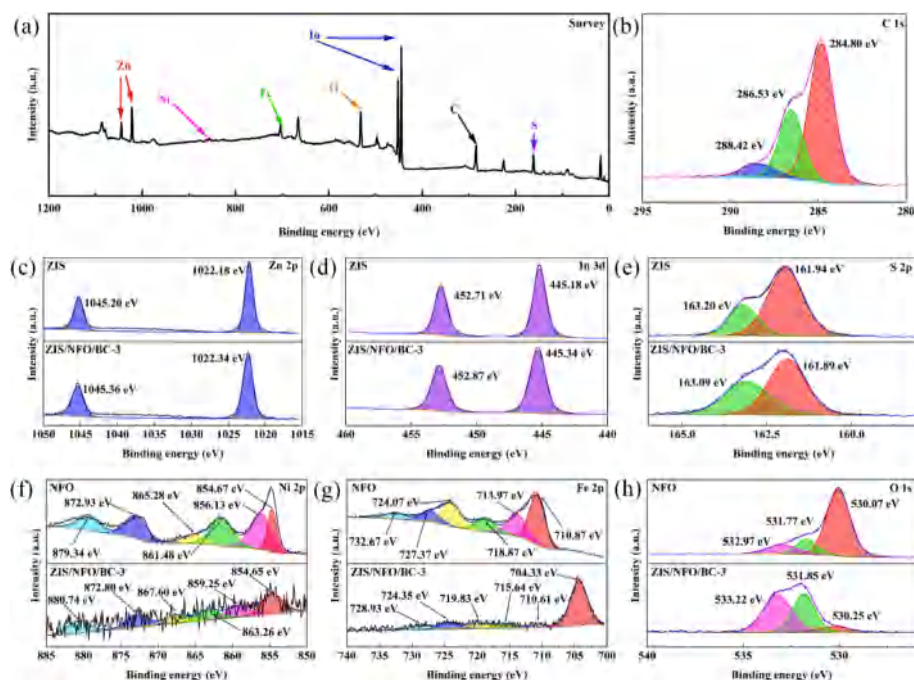
Fig. 4. XPS spectra of ZIS, NFO, ZIS/NFO/BC-3: (a) survey of ZIS/NFO/BC-3; (b) C 1 s; (c) Zn 2p; (d) In 3d; (e) S 2p; (f) Ni 2p; (g) Fe 2p; (h) O 1 s.

presents two main peaks at 724.07 and 710.87 eV, referring to Fe $2p_{1/2}$ and Fe $2p_{3/2}$, respectively, also along with the satellite peaks [42,43]. As for ZIS/NFO/BC-3, the peaks in Ni and Fe spectra shifted to lower BE values. This peak shift results were consistent with other literatures, which reported that the change can be ascribed to the formation of p-n junction [44]. The incorporation of BC resulted in strong connection between C (from BC) and Fe (from NFO) elements, which led to more negative shift of the peaks in Fe 2p spectrum, due to the electron movement between biochar and ferrite [45].

In Fig. 4h, the O 1 s spectrum of NFO is resolved into three peaks. The

strongest peak appears at the BE of 530.07 eV, corresponding to lattice oxygen [46]. The other two peaks at 531.77 and 532.97 eV can be designated to the surface –OH group [47] and metal–oxygen bond, respectively [48]. However, the peaks in the O 1 s spectrum of ZIS/NFO/BC-3 all appear at higher BE values. The peak at 530.25 eV can be attributed to lattice oxygen from NFO. The intensity of this peak is very weak, implying the tiny amount of NFO particles in ZIS/NFO/BC-3. The peak at 531.85 eV is ascribed to C=O and –OH from biochar [49], and the peak at 533.22 eV is attributed to C—O bond from biochar [45]. The positive shift of these peaks can be explained as follows. In the NFO
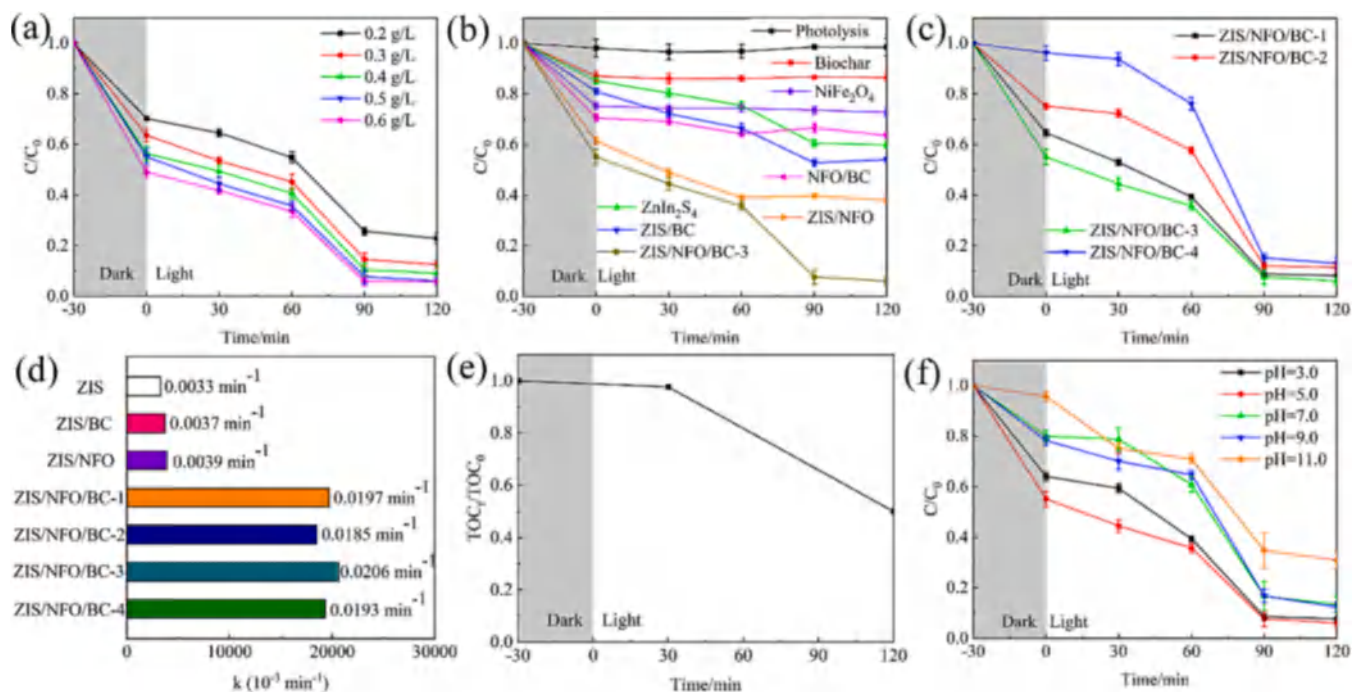

Fig. 5. The change of concentration ratio of DOXH solution: (a) via catalysts of different dosages; (b) using different samples; (c) using ZIS/NFO/BC-*x*; (d) the corresponding reaction rate constant values; (e) the TOC ratios at different reaction time; (f) the effect of initial pH values of DOXH solution.

samples, the main role of oxygen is lattice oxygen, however in ZIS/NFO/BC-3, due to the large proportion of biochar and tiny content of NFO, the peaks reflecting biochar appeared as typical ones and the characteristic peaks of NFO disappeared. This result also implies the abundant oxygen-containing functional groups on the surface of biochar [50].

3.5. Photodegradation activity evaluation

The photodegradation performances of reported catalyst and related samples were studied via the degradation of DOXH under simulated sunlight (Section 2.3.). First, the optimal catalyst amount was determined using ZIS/NFO/BC-3, and the result is presented in Fig. 5a, in which the concentration ratio reflects the photodegradation efficiency. Fig. 5a implies that 0.5 g/L was the optimal catalyst dosage, probably due to the photo-shielding effect of overdose that hindered photocatalytic activity.

Second, the comparison of photodegradation efficiencies of all samples were presented in Fig. 5b. The photodegradation of DOXH itself can be ignored (photolysis). Biochar (BC), NiFe$_2$O$_4$ (NFO) and NFO/BC showed certain adsorption towards DOXH, but no photodegradation can be observed. Among those photocatalytic samples, pure ZnIn$_2$S$_4$ (ZIS) showed the weakest photodegradation efficiency, while the ternary-one showed the strongest. This can be ascribed to the synergy between biochar, ZIS and NFO. The comparison between different ternary catalysts is shown in Fig. 5c, which presents that ZIS/NFO/BC-3 was the optimal sample. Higher amount of NFO on the surface of BC reduced the specific surface area and shielded active sites, which lowered the photocatalytic efficiency.

The comparison of these photocatalytic samples can be further illustrated by kinetics, using pseudo-first-order kinetic equation as follows:

$$ln(\frac{C_0}{C}) = kt \tag{1}$$

In which k, C, C_0 and t represent the apparent reaction rate constant, DOXH concentration, initial DOXH concentration and reaction time, respectively. The k values are presented in Fig. 5d, which was consistent with the above viewpoint.

Above all, about 94.0 % of doxycycline (30 mg/L) was degraded within 120 min using 0.5 g/L of ZIS/NFO/BC-3 photocatalyst. This result is efficient when compared with similar literatures. Table S3 listed the comparison of the reports on photocatalysts for doxycycline removal.

The TOC (total organic carbon) ratio during photodegradation reflects the mineralization of DOXH. As shown in Fig. 5e, the TOC ratio kept almost constant after dark (adsorption) and 30 min of irradiation. However, this value dropped to 0.50 after photodegradation of 2 h, reflecting a great part of DOXH was degraded into harmless CO$_2$ released into air, which greatly reduced the overall threat to aquatic environment.

3.6. Impact of water quality parameters

Real water matrix is much more complicated then DOXH solution prepared by deionized water. Some of the typical parameters that might affect photodegradation efficiency are: pH value, coexisting ions, natural organic matter.

The effect of initial pH value of DOXH solution was evaluated, as presented in Fig. 5f, which exhibits that pH = 5.0 showed the slightest effect. This can be ascribed to two factors: one is the surface charge of photocatalyst, the other is the form of DOXH at different pH conditions [51]. As presented in Fig. S3, the zeta potential of ZIS/NFO/BC-3 is 2.77, which means the negative surface charge of biochar became stronger when pH value increased from 3 to 11. Meanwhile, since the pKa values of DOXH are 3.5, 7.7 and 9.5, DOXH existed as cations when pH was lower than 3.5, and electrically neutral when pH was between 3.5 and

7.7, and anion when pH was higher than 7.7 [52]. Thus, when pH was 9.0 or 11.0, the intense repulsion between photocatalyst and DOXH hindered the adsorption, thus reduced photodegradation efficiency [53]. When pH was 7.0, the strong negative surface of photocatalyst also hindered the attachment of DOXH molecules, resulting in reduced photodegradation efficiency. This explains why the initial pH values showed weak effect when its value was 3.0 or 5.0.

The effects of coexisting ions on photodegradation efficiency were evaluated. Fig. 6a presents the effect of Cl$^-$ anion with varied concentration. It can be noticed that Cl$^-$ showed slight effect on photodegradation removal of DOXH, regardless of different concentrations. Fig. 6b shows the effect of NO$_3^-$ with varied concentration. The result was similar to that of Cl$^-$ anion. These results were consistent with related literatures [54,55]. Fig. 6c shows the effect of CO$_3^{2-}$ with varied concentration. It is obvious that CO$_3^{2-}$, regardless of different concentrations, greatly hindered the photodegradation reaction. CO$_3^{2-}$ can partly transform into HCO$_3^-$, and both anions could act as radical scavengers and remove the reactive species involved in the photodegradation reaction [56]. This resulted in the decrease of photodegradation efficiency.

The effect of natural organic matter (NOM) was also studied, and humic acid (HA) was selected since it's a typical NOM. Fig. 6d shows the effect of HA with varied concentration. It is noticed that HA with different concentrations greatly inhibited photodegradation reaction. First, HA anions were adsorbed onto the surface of ZIS/NFO/BC-3, which resulted in the competition for adsorption sites [57]. Second, HA anions might partly block the micropores of photocatalyst, resulting in reduced specific surface area and thus weakened the adsorption ability of photocatalyst [58]. Third, the number of photons reached onto the surface of photocatalyst decreased due to the brown color of HA anions [59]. All these factors greatly hindered the photocatalytic activity of ZIS/NFO/BC-3.

3.7. Photodegradation mechanism investigation

The photodegradation efficiency using photocatalyst is often related to its physicochemical properties: light response ability, surface condition and photo-induced charge carrier mobility and recombination. Thus, in this paper, all these aspects are discussed.

Fig. 7 exhibits the UV–vis DRS spectra of biochar, ZIS, NFO, ZIS/NFO and ZIS/NFO/BC-3, reflecting their light-absorption ability. The black biochar exhibits high absorption towards both UV and visible light. Pure ZIS exhibits intense absorption to UV light, and good absorption at the wavelength below 550 nm. The black NFO also exhibits high absorption to UV and visible light, with the typical spectrum similar to other related literature [60]. ZIS/NFO shows high absorption intensity towards UV light, and relatively low intensity in visible light region. The shape of its spectrum is similar to the spectra of ZIS and NFO. The ternary ZIS/NFO/BC-3 exhibits relatively low intensity in UV region, but very strong absorption towards visible light. This is beneficial to photodegradation performance, since visible light is the main part of sunlight. Above all, it is reasonable to speculate that light response ability is one essential factor that affects photocatalytic activity. The band gap (E$_g$) value of ZIS can be estimated as 2.30 eV (Fig. 7b), and the E$_g$ value of NFO is 1.50 eV (Fig. 7c). For reference, the photos of above-mentioned samples are presented in Fig. 7d.

It is well-known that larger specific surface area means more adsorption sites and active spots for reaction, thus contributing to better photodegradation performance [61–63]. Fig. 8a exhibits the nitrogen absorption–desorption isotherms of biochar and ZIS/NFO/BC-3, from which their S$_{BET}$ (Brunauer-Emmett-Teller surface area) values can be deduced as 12.73 and 89.76 m^2/g, respectively. Fig. 8b shows the corresponding pore size distribution of both samples, reflecting that ZIS/NFO/BC-3 has higher pore volume than biochar, probably due to the combination of ZIS and NFO particles. These results imply that the better surface condition of ZIS/NFO/BC-3 is beneficial to photodegradation performance.
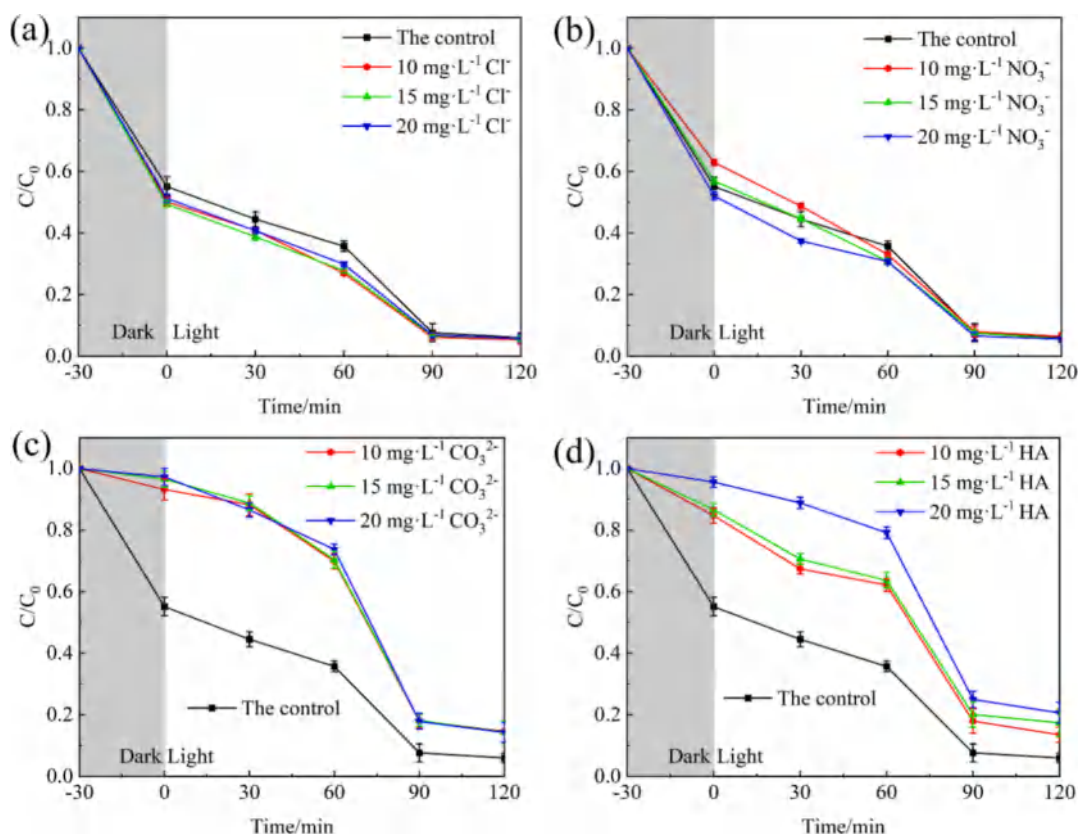
Fig. 6. The effects of (a) Cl^-, (b) NO_3^-, (c) CO_3^{2-} and (d) HA on the concentration change of DOXH solution.
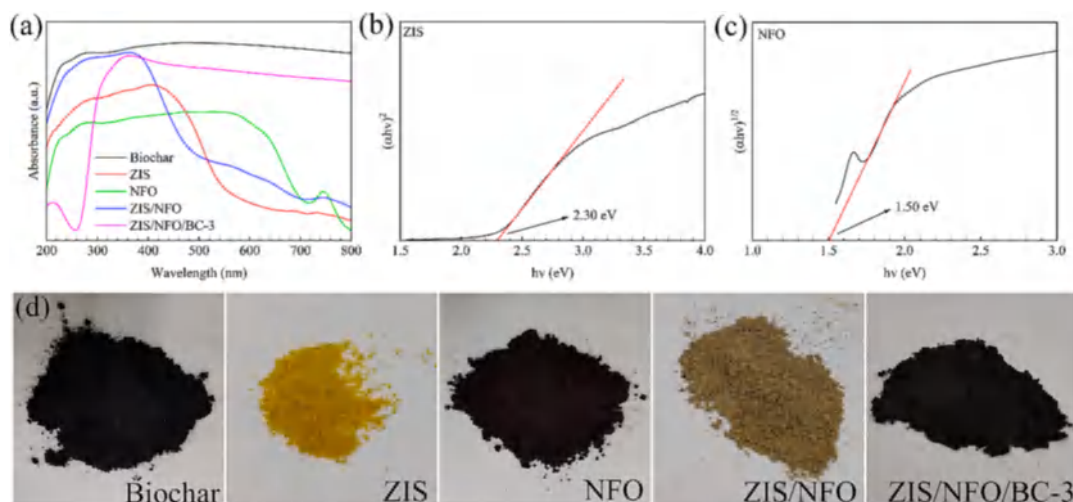

Fig. 7. (a) UV–vis DRS of biochar, ZIS, NFO, ZIS/NFO and ZIS/NFO/BC-3; (b-c) Tauc plots of ZIS and NFO; (d) the photos of biochar, ZIS, NFO, ZIS/NFO and ZIS/NFO/BC-3.

The charge carrier mobility can be evaluated by photoluminescence (PL) and electrochemical methods. The PL spectra of ZIS, ZIS/NFO and ZIS/NFO/BC-3 are presented in Fig. 9a. These spectra reflect the recombination of photo-induced electron-hole pairs, that is, the higher intensity of the spectra, the faster recombination between electrons and holes, which led to reduced photocatalytic efficiency. ZIS/NFO/BC-3 presented the lowest intensity compared to ZIS/NFO and ZIS, meaning that the recombination of electron-hole pairs was greatly hindered due to the p-n heterojunction structure, as well as substrate biochar, which promoted charge carrier mobility due to its good electric conductivity.

More evidences can be obtained from electrochemical results. The photocurrent (PC) spectra are shown in Fig. 9b, reflecting similar trends to that of PL result. When irradiation is on, photocurrent can be observed and ZIS/NFO/BC-3 exhibited highest current intensity, reflecting its highest photocatalytic activity. The Electrochemical Impedance Spectroscopy (EIS) spectra shown in Fig. 9c indicate that, a much smaller arc radius of ZIS/NFO/BC-3 spectrum can be observed, reflecting its high separation efficiency of electron-hole pairs. Above all, the recombination of charge carriers can be greatly inhibited, due to the charge carrier separation at p-n junction interface. Also, as an electron mediator, biochar promoted charge carrier transfer due to its typical interconnected structure, as well as good electric conductivity. All these factors greatly
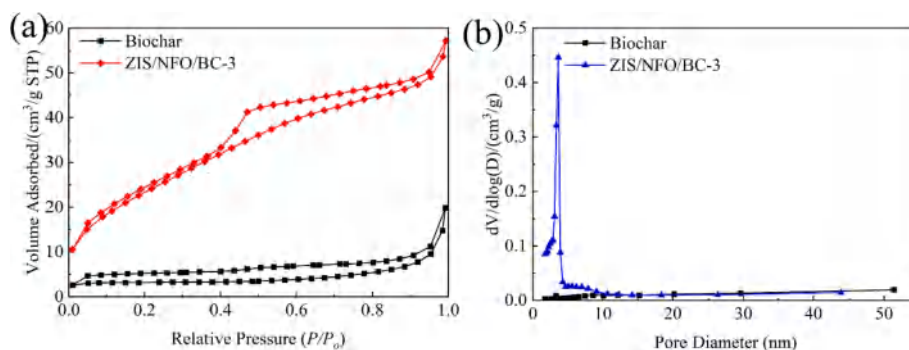
Fig. 8. (a) Nitrogen adsorption–desorption isotherms and (b) pore size distribution of biochar and ZIS/NFO/BC-3.
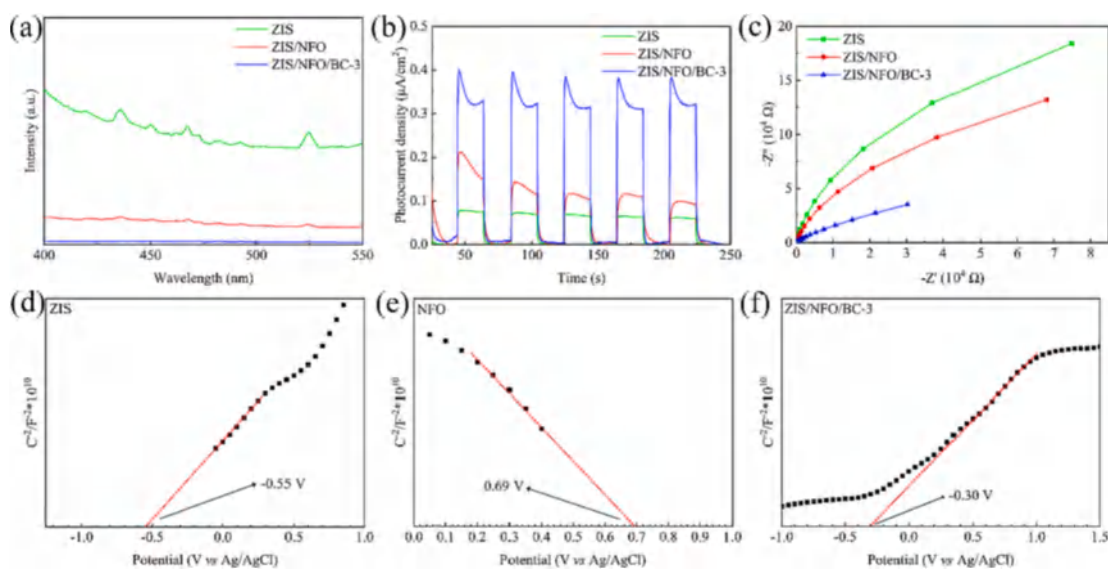

Fig. 9. (a) The PL, (b) photocurrent and (c) EIS spectra of ZIS, ZIS/NFO and ZIS/NFO/BC-3; Mott-schottky plots of (d) ZIS, (e) NFO and (f) ZIS/NFO/BC-3.

enhanced photocatalytic activity.

Moreover, fluorescence decay experiments were carried out to further clarify the charge transfer and separation. As shown in Fig. S4a-b, the fluorescence decay curves of ZIS and ZIS/NFO were fitted and the average lifetime (τ_{ave}) were estimated by the following equation.

$$\tau_{ave} = (A_1\tau_1 + A_2\tau_2)/(A_1 + A_2) \qquad (2)$$

According to the results, the τ_{ave} of ZIS/NFO (0.71 ns) is shorter than that of pristine ZIS (1.11 ns). The decrease compared to ZIS implies that photo-induced charge carriers moved efficiently at the interface inside ZIS/NFO. This result proves the advantage of p-n junction, which can effectively hinder charge carrier recombination and improve photocatalytic activity.

As it has been mentioned above, the bandgap (E_g) values of ZIS and NFO are 2.30 eV and 1.50 eV, respectively. Based on the valence band maximum XPS spectra of ZIS and NFO (Fig. S5a,b), The valence band potential (E_{VB}) of ZIS and NFO can be estimated as 1.80 eV and 1.10 eV, respectively. According to the following equation, the conduction band potential (E_{CB}) of ZIS and NFO can be calculated to be −0.50 eV and −0.40 eV, respectively.

$$E_{VB} = E_{CB} + E_g \qquad (3)$$

Another useful data from electrochemical analysis are the Mott-Schottky (MS) plots, from which the flat-band potential (E_{FB}) of ZIS and NFO can be determined. The MS plot of ZIS is shown in Fig. 9d, the slope of which is positive, reflecting that it's a *n*-type semiconductor [64]. Its E_{FB} is −0.55 V *vs* Ag/AgCl. The MS plot of NFO is shown in

Fig. 9e, the slope of which is negative, implying that it's a p-type semiconductor [19]. Its E_{FB} is 0.69 V *vs* Ag/AgCl. The E_{FB} values of ZIS and NFO can be converted to −0.35 eV and 0.89 eV (*vs* NHE), respectively. Fig. 9f shows that the E_{FB} of ZIS/NFO/BC-3 moved to −0.30 V *vs* Ag/AgCl, due to the formation of p-n junction, which led to a shift of flat-band potential [65].

The scavenging test results of ZIS/NFO/BC-3 are present in Fig. 11d. When EDTA-2Na was introduced, the photodegradation efficiency dropped to the lowest, implying that h⁺ was the major ROS. Meanwhile, the photodegradation efficiency also reduced when BQ was added, which implies that ·O₂⁻ played a secondary role during photodegradation. It is also notable that ·OH did not make any contribution to photodegradation. In conclusion, h⁺ and ·O₂⁻ were the main ROS during DOXH photodegradation by ZIS/NFO/BC.

All the above contents provide information that can be used to propose photodegradation mechanism, as shown in Fig. 10. Before contact, the energy states of pure ZIS and NFO are presented in the left part of the diagram. After contact, a p-n junction was formed, and the flat bands of ZIS and NFO moved up and down until an internal electric field was formed at the interface, due to the mutual charge transfer [66], where negative charge carriers in ZIS migrated to p-type NFO, and positive charge carriers migrated from p-type NFO to *n*-type ZIS (the middle part of the diagram). When ZIS/NFO/BC was irradiated by sunlight, photo-induced electrons moved from CB of NFO to CB of ZIS, while the photo-induced holes moved from VB of ZIS to VB of NFO (the right part of the diagram). This charge carrier migration greatly hindered the recombination, promoting photocatalytic activity and
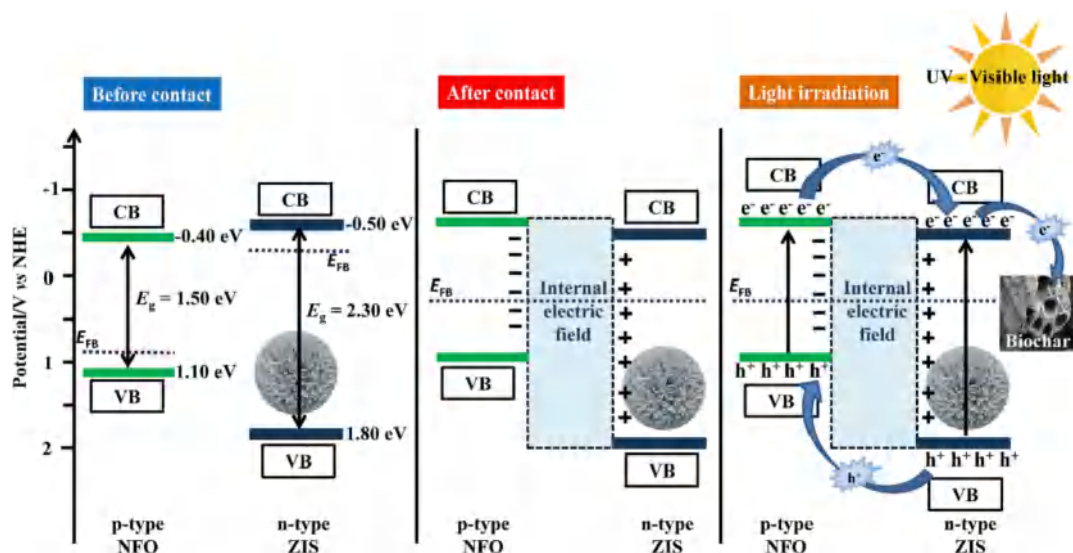
Fig. 10. Proposed mechanism for DOXH photodegradation using ZIS/NFO/BC under simulated sunlight.
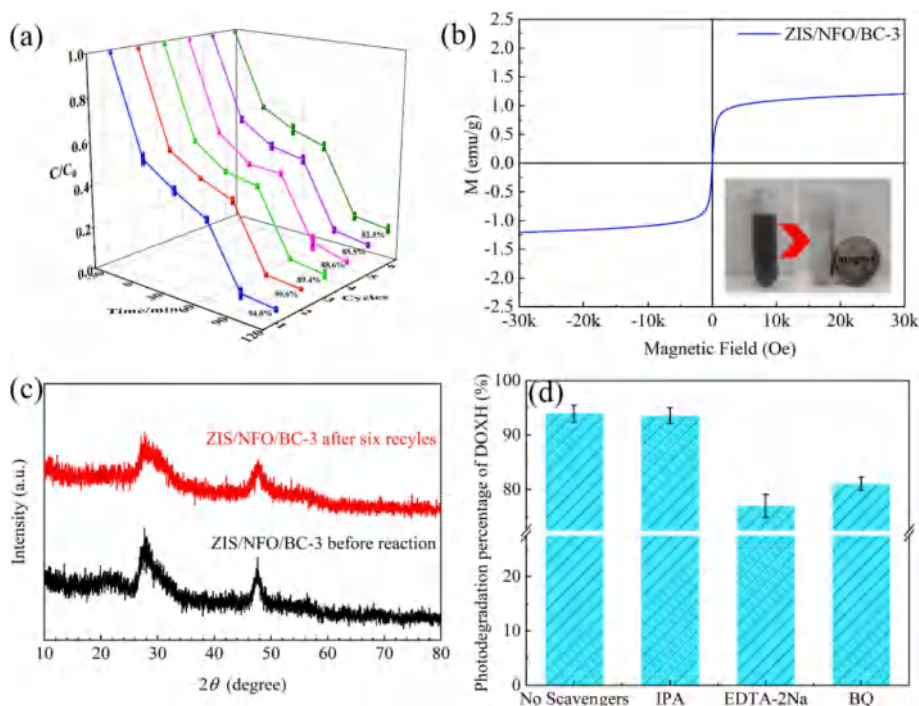

Fig. 11. (a) The reusing test results of ZIS/NFO/BC-3; (b) the magnetic hysteresis loops of ZIS/NFO/BC-3 at room temperature (inset: the magnetic separation after photodegradation test using ZIS/NFO/BC-3); (c) the XRD patterns of ZIS/NFO/BC-3 before and after the recycling tests; (d) the concentration ratio of DOXH solution during scavenging tests.

preventing the photo-corrosion of ZIS particles. This ensured its long-term photodegradation application (this will be discussed in the following section).

The role of biochar is very important, and can be illustrated by the following aspects. First, its wide light-absorption region (UV & Visible light) ensured efficient utilization of sunlight, a key factor that promoted photocatalytic activity. Second, its porous structure optimized the morphology of ZIS/NFO/BC, which not only prevented nanoparticle aggregation but also enhanced adsorption ability towards DOXH. Third, the synergy of "adsorption & degradation" resulted in enhanced photodegradation efficiency. Fourth, its excellent electric conductivity promoted the migration of photo-induced electrons, greatly hindered charge carrier recombination, which is also beneficial to

photodegradation. The enhanced electron migration also facilitated the conversion from O_2 to $\cdot O_2^-$, which was the ROS during photodegradation.

The energy band alignment of ZIS/NFO/BC composite can be further confirmed for verifying the proposed mechanism. The conduction-band offset (ΔE_{CBO}) and valence-band offset (ΔE_{VBO}) of p-n junction can be estimated by the following equations [44,67]:

$$\Delta E_{VBO} = (E_{Ni,2p} - E_{V,Ni})^{NFO}_{pure} - (E_{In,3d} - E_{V,In})^{ZIS}_{pure} + \Delta E_{CL} \tag{4}$$

$$\Delta E_{CBO} = E_g^{NFO} - E_g^{ZIS} + \Delta E_{VBO} \tag{5}$$

$$\Delta E_{CL} = (E_{In,3d} - E_{Ni,2p})^{ZIS/NFO/BC}_{p-n\ junction} \tag{6}$$

In these equations, $E_{Ni,2p}$ and $E_{In,3d}$ are the binding energy (BE) values of pristine NFO and ZIS, respectively; while $E_{V,Ni}$ and $E_{V,In}$ are the valence band maximum (VBM) positions of NFO and ZIS, respectively. $E_{g(ZIS)}$ and $E_{g(NFO)}$ are the band gap values of ZIS and NFO, respectively. ΔE_{CL} is the energy between Ni 2p and In 3d core levels in p-n heterojunction. The core level positions can be determined by XPS method. The VBM positions of ZIS and NFO are estimated based on valence band maximum XPS spectra. The $E_{g(ZIS)}$ and $E_{g(NFO)}$ are estimated based on the UV–vis DRS spectra.

As presented in Fig. S6, the $E_{g(ZIS)}$ and $E_{g(NFO)}$ values are 2.30 eV and 1.50 eV, respectively. The values between VBM and core-level positions for ZIS and NFO are 443.38 and 853.57 eV, respectively. The value between Ni 2p and In 3d core levels in p-n heterojunction is 409.31 eV. The BE values for the core-level, VBM, and band gap of pristine ZIS, NFO and p-n heterojunction are summarized in Table S4. Based on these data, the ΔE_{VBO} and ΔE_{CBO} values for p-n heterojunction are estimated to be 0.88 eV and 0.08 eV, respectively. The positive difference means that the CB and VB positions of NFO are higher than that of ZIS. These results imply that type-II band alignment of p-n junction can be observed (Fig. 10) [68], where photo-induced holes migrate from VB of ZIS to VB of NFO, while photo-induced electrons move from CB of NFO to CB of ZIS, driven by band energetics [67].

3.8. Reusability evaluation

The reusability of ZIS/NFO/BC-3 was evaluated, as well as its stability. As shown in Fig. 11a, after six cycles, the DOXH photodegradation percentage slightly dropped from 94.0 % to 82.5 %. This can be attributed to the weight loss during separation and recovery period. The ternary photocatalyst can simply be collected from water phase by an external magnet (inset of Fig. 11b) due to its superparamagnetism (Fig. 11b). The ZIS/NFO/BC-3 after six cycles was characterized by XRD. As shown in Fig. 11c, the crystal structure of ZIS/NFO/BC-3 had no apparent changes. Thus, it is considered reasonable that ZIS/NFO/BC exhibited good chemical stability and reusability.

3.9. Photodegradation intermediates and possible pathway investigation

Since the TOC ratio is much lower than DOXH concentration ratio during photodegradation, it can be deduced that various intermediates were generated during this period. HPLC-MS method was applied to find out the possible form of these intermediates. As presented in Fig. 12, there are three pathways. For pathway-one, the demethylation of DOXH resulted in the formation of intermediate A, which converted to intermediate B due to deamidation. And then, ring-opening process took place, turning intermediate B into C. For pathway-two, dehydroxylation process turned DOXH into intermediate D, which then transformed to intermediate E by demethylation. The ring-opening reaction further converted it into intermediate F. The hydroxylation and detachment of carboxyl group turned it into intermediate G, which also originated from intermediate C. The dehydroxylation process turned intermediate G into intermediate H, I and J. For pathway-three, DOXH can be converted into intermediate K through ring-opening reaction. The reaction that turned acylamide group into carboxyl group resulted in the formation of intermediate L. The ring-opening reaction and functional group detachment turned intermediate L into intermediate P and Q, which further transformed into fatty alcohol (intermediate R) and alkane (intermediate S).

4. Conclusion

This work reported the fabrication and photodegradation performance of a novel photocatalyst, built from $ZnIn_2S_4/NiFe_2O_4$ p-n junction and biochar. Based on DOXH photodegradation data, the optimal photocatalyst sample and dosage were determined, and the effects of pH value, coexisting ions and humic acid were evaluated. The superior photodegradation performance of ZIS/NFO/BC-3 can be ascribed to the synergy between biochar, ZIS and NFO. The light response ability, electron conductivity and adsorption capability of biochar improved photodegradation efficiency. The ZIS/NFO p-n junction also promoted photodegradation performance due to prolonged charge carrier lifetime. Photo-induced holes were determined as the major ROS during photodegradation. The photodegradation mechanism, possible reaction
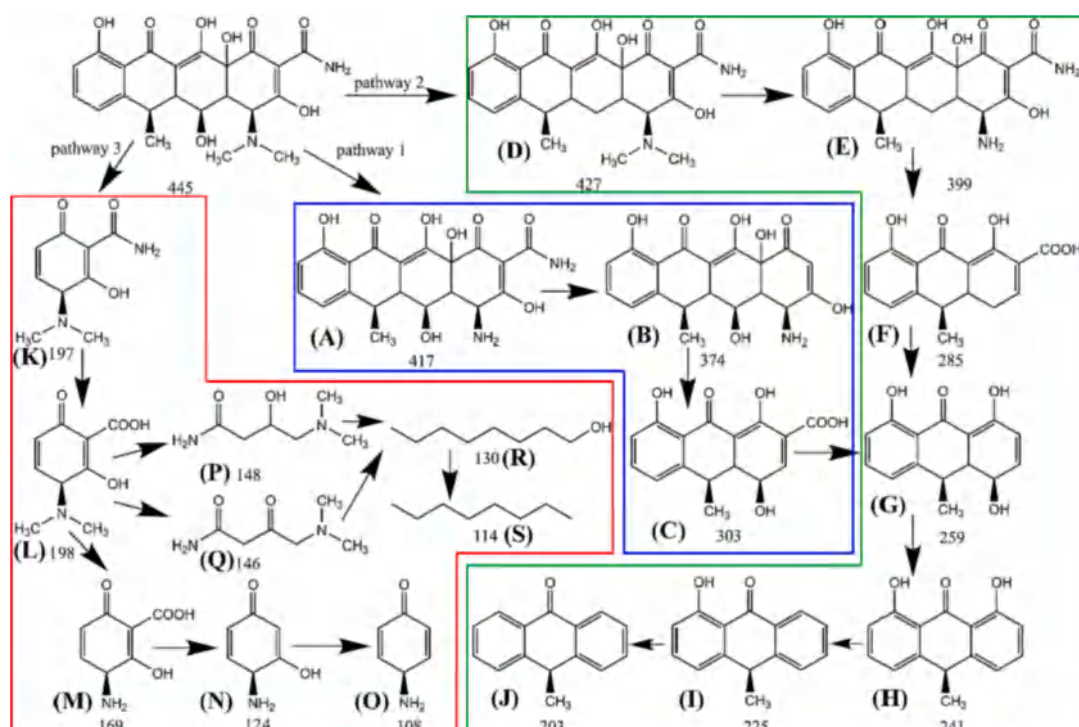

Fig. 12. Possible photodegradation pathways and intermediates using ZIS/NFO/BC.

pathway and intermediates were proposed based on characterization and degradation results. The reported ZIS/NFO/BC can simply be collected via magnet, exhibiting good stability and reusability after six cycles. This reported ternary composite can be considered as a promising route for the development of novel photocatalyst for wastewater treatment.

CRediT authorship contribution statement

Qiong Wu: Conceptulization, Data curation, Formal analysis, Investigation, Writing - original draft. **Youtao Song:** Supervision, Conceptualization, Funding acquisition, Writing - review & editing.

Declaration of Competing Interest

The authors declare that they have no known competing financial interests or personal relationships that could have appeared to influence the work reported in this paper.

Data availability

Data will be made available on request.

Acknowledgements

Appendix A. Supplementary data

Supplementary data to this article can be found online at https://doi.org/10.1016/j.cej.2022.139745.

References

[1] B.W. Wang, H.J. Su, B. Zhang, Hydrodynamic cavitation as a promising route for wastewater treatment - A review, Chem. Eng. J. 412 (2021), https://doi.org/10.1016/j.cej.2021.128685.

[2] K. Fedorov, K. Dinesh, X. Sun, R.D.C. Soltani, Z.H. Wang, S. Sonawane, G. Boczkaj, Synergistic effects of hybrid advanced oxidation processes (AOPs) based on hydrodynamic cavitation phenomenon - A review, Chem. Eng. J. 432 (2022), https://doi.org/10.1016/j.cej.2021.134191.

[3] P. Liu, L. Qian, H.Y. Wang, X. Zhan, K. Lu, C. Gu, S.X. Gao, New Insights into the Aging Behavior of Microplastics Accelerated by Advanced Oxidation Processes, Environ. Sci. Technol. 53 (7) (2019) 3579–3588, https://doi.org/10.1021/acs.est.9b00493.

[4] Q. Yang, Y. Ma, F. Chen, F. Yao, J. Sun, S. Wang, K. Yi, L. Hou, X. Li, D. Wang, Recent advances in photo-activated sulfate radical-advanced oxidation process (SR-AOP) for refractory organic pollutants removal in water, Chem. Eng. J. 378 (2019), 122149, https://doi.org/10.1016/j.cej.2019.122149.

[5] A. Gupta, A. Garg, Degradation of ciprofloxacin using Fenton's oxidation: Effect of operating parameters, identification of oxidized by-products and toxicity assessment, Chemosphere 193 (2018) 1181–1188, https://doi.org/10.1016/j.chemosphere.2017.11.046.

[6] G. Li, Y. Feng, B. Wang, M. Wang, Contribution of hydroxyl radicals to the degradation of Acid Orange 7 by fly ash under ultrasonic irradiation, Desalin. Water Treat. 57 (39) (2015) 18168–18174, https://doi.org/10.1080/19443994.2015.1089196.

[7] C. Lai, N. An, B.S. Li, M.M. Zhang, H. Yi, S.Y. Liu, L. Qin, X.G. Liu, L. Li, Y.K. Fu, F. H. Xu, Z.H. Wang, X.X. Shi, Z.W. An, X.R. Zhou, Future roadmap on nonmetal-based 2D ultrathin nanomaterials for photocatalysis, Chem. Eng. J. 406 (2021) 24, https://doi.org/10.1016/j.cej.2020.126780.

[8] P. Li, Z. Zhou, Q. Wang, M. Guo, S. Chen, J. Low, R. Long, W. Liu, P. Ding, Y. Wu, Y. Xiong, Visible-light-driven nitrogen fixation catalyzed by Bi₅O₇Br Nanostructures: Enhanced Performance by Oxygen Vacancies, J. Am. Chem. Soc. 142 (28) (2020) 12430–12439, https://doi.org/10.1021/jacs.0c05097.

[9] S. Wang, B.Y. Guan, X. Wang, X.W.D. Lou, Formation of Hierarchical Co₉S₈@ ZnIn₂S₄ Heterostructured Cages as an Efficient Photocatalyst for Hydrogen Evolution, J. Am. Chem. Soc. 140 (45) (2018) 15145–15148, https://doi.org/10.1021/jacs.8b07721.

[10] W. Chen, L. Chang, S.-B. Ren, Z.-C. He, G.-B. Huang, X.-H. Liu, Direct Z-scheme 1D/2D WO₂.₇₂/ZnIn₂S₄ hybrid photocatalysts with highly-efficient visible-light-driven photodegradation towards tetracycline hydrochloride removal, J. Hazard. Mater. 384 (2020), 121308, https://doi.org/10.1016/j.jhazmat.2019.121308.

[11] H. Li, P. Wang, X. Yi, H. Yu, Edge-selectively amidated graphene for boosting H₂-evolution activity of TiO₂ photocatalyst, Appl. Catal. B 264 (2020), 118504.

[12] K. Zhu, J. Ou-Yang, Q. Zeng, S. Meng, W. Teng, Y. Song, S. Tang, Y. Cui, Fabrication of hierarchical ZnIn₂S₄@CNO nanosheets for photocatalytic hydrogen production and CO₂ photoreduction, Chin. J. Catal. 41 (3) (2020) 454–463, https://doi.org/10.1016/S1872-2067(19)63494-7.

[13] Z. Yi, J. Ye, N. Kikugawa, T. Kako, S. Ouyang, H. Stuart-Williams, H. Yang, J. Cao, W. Luo, Z. Li, Y. Liu, R.L. Withers, An orthophosphate semiconductor with photooxidation properties under visible-light irradiation, Nat. Mater. 9 (7) (2010) 559–564, https://doi.org/10.1038/nmat2780.

[14] Y. Song, J. Zhang, X. Dong, H. Li, A Review and Recent Developments in Full-Spectrum Photocatalysis using ZnIn₂S₄-Based Photocatalysts, Energy Technology 9 (5) (2021) 2100033, https://doi.org/10.1002/ente.202100033.

[15] W. Yang, L. Zhang, J. Xie, X. Zhang, Q. Liu, T. Yao, S. Wei, Q. Zhang, Y. Xie, Enhanced Photoexcited Carrier Separation in Oxygen-Doped ZnIn₂S₄ Nanosheets for Hydrogen Evolution, Angew. Chem. Int. Ed. 55 (23) (2016) 6716–6720, https://doi.org/10.1002/anie.201602543.

[16] T. Zhu, X. Ye, Q. Zhang, Z. Hui, X. Wang, S. Chen, Efficient utilization of photogenerated electrons and holes for photocatalytic redox reactions using visible light-driven Au/ZnIn₂S₄ hybrid, J. Hazard. Mater. 367 (2019) 277–285, https://doi.org/10.1016/j.jhazmat.2018.12.093.

[17] H. Yang, R. Cao, P. Sun, J. Yin, S. Zhang, X. Xu, Constructing electrostatic self-assembled 2D/2D ultra-thin ZnIn₂S₄/protonated g-C₃N₄ heterojunctions for excellent photocatalytic performance under visible light, Appl. Catal. B 256 (2019), 117862, https://doi.org/10.1016/j.apcatb.2019.117862.

[18] C. Li, H. Che, P. Huo, Y. Yan, C. Liu, H. Dong, Confinement of ultrasmall CoFe₂O₄ nanoparticles in hierarchical ZnIn₂S₄ microspheres with enhanced interfacial charge separation for photocatalytic H₂ evolution, J. Colloid Interface Sci. 581 (Pt B) (2021) 764–773, https://doi.org/10.1016/j.jcis.2020.08.019.

[19] W. Fu, X. Xu, W. Wang, J. Shen, M. Ye, In-Situ Growth of NiFe₂O₄/2D MoS₂ p-n Heterojunction Immobilizing Palladium Nanoparticles for Enhanced Visible-Light Photocatalytic Activities, ACS Sustainable Chem. Eng. 6 (7) (2018) 8935–8944, https://doi.org/10.1021/acssuschemeng.8b01299.

[20] Y.-J. Yuan, J.-R. Tu, Z.-J. Ye, D.-Q. Chen, B. Hu, Y.-W. Huang, T.-T. Chen, D.-P. Cao, Z.-T. Yu, Z.-G. Zou, MoS₂-graphene/ZnIn₂S₄ hierarchical microarchitectures with an electron transport bridge between light-harvesting semiconductor and cocatalyst: A highly efficient photocatalyst for solar hydrogen generation, Appl. Catal. B 188 (2016) 13–22, https://doi.org/10.1016/j.apcatb.2016.01.061.

[21] M.E. Borges, M. Sierra, E. Cuevas, R.D. García, P. Esparza, Photocatalysis with solar energy: Sunlight-responsive photocatalyst based on TiO₂ loaded on a natural material for wastewater treatment, Sol. Energy 135 (2016) 527–535, https://doi.org/10.1016/j.solener.2016.06.022.

[22] R. Shan, J. Han, J. Gu, H. Yuan, B. Luo, Y. Chen, A review of recent developments in catalytic applications of biochar-based materials, Resour. Conserv. Recycl. 162 (2020), 105036, https://doi.org/10.1016/j.resconrec.2020.105036.

[23] X. Zhou, Y. Zhu, Q. Niu, G. Zeng, C. Lai, S. Liu, D. Huang, L. Qin, X. Liu, B. Li, H. Yi, Y. Fu, L. Li, M. Zhang, C. Zhou, J. Liu, New notion of biochar: A review on the mechanism of biochar applications in advannced oxidation processes, Chem. Eng. J. 416 (2021), 129027, https://doi.org/10.1016/j.cej.2021.129027.

[24] C. Yang, Q. Li, Y. Xia, K. Lv, M. Li, Enhanced visible-light photocatalytic CO₂ reduction performance of ZnIn₂S₄ microspheres by using CeO₂ as cocatalyst, Appl. Surf. Sci. 464 (2019) 388–395, https://doi.org/10.1016/j.apsusc.2018.09.099.

[25] M. Nawaz, A. Shahzad, K. Tahir, J. Kim, M. Moztahida, J. Jang, M.B. Alam, S.-H. Lee, H.-Y. Jung, D.S. Lee, Photo-Fenton reaction for the degradation of sulfamethoxazole using a multi-walled carbon nanotube-NiFe₂O₄ composite, Chem. Eng. J. 382 (2020), 123053, https://doi.org/10.1016/j.cej.2019.123053.

[26] M. Nadafan, M. Parishani, Z. Dehghani, J.Z. Anvari, R. Malekfar, Third-order nonlinear optical properties of NiFe₂O₄ nanoparticles by Z-scan technique, Optik 144 (2017) 672–678, https://doi.org/10.1016/j.ijleo.2017.06.128.

[27] J.T. Adeleke, T. Theivasanthi, M. Thiruppathi, M. Swaminathan, T. Akomolafe, A. B. Alabi, Photocatalytic degradation of methylene blue by ZnO/NiFe₂O₄ nanoparticles, Appl. Surf. Sci. 455 (2018) 195–200, https://doi.org/10.1016/j.apsusc.2018.05.184.

[28] S. Zhang, M. Du, Z. Xing, Z. Li, K. Pan, W. Zhou, Defect-rich and electron-rich mesoporous Ti-MOFs based NH₂-MIL-125(Ti)@ZnIn₂S₄/CdS hierarchical tandem heterojunctions with improved charge separation and enhanced solar-driven photocatalytic performance, Appl. Catal. B 262 (2020), 118202, https://doi.org/10.1016/j.apcatb.2019.118202.

[29] J. Tang, N. Zhu, Y. Zhu, P. Kerr, Y. Wu, Distinguishing the roles of different extracellular polymeric substance fractions of a periphytic biofilm in defending against Fe₂O₃ nanoparticle toxicity, Environ. Sci. Nano 4 (8) (2017) 1682–1691.

[30] A.C. Fröhlich, E.L. Foletto, G.L. Dotto, Preparation and characterization of NiFe₂O₄/activated carbon composite as potential magnetic adsorbent for removal of ibuprofen and ketoprofen pharmaceuticals from aqueous solutions, J. Cleaner Prod. 229 (2019) 828–837, https://doi.org/10.1016/j.jclepro.2019.05.037.

[31] D. Creanga, G. Calugaru, Physical investigations of a ferrofluid based on hydrocarbons, J. Magn. Magn. Mater. 289 (2005) 81–83, https://doi.org/10.1016/j.jmmm.2004.11.023.

[32] S. Dey, J. Ghose, Synthesis, characterisation and magnetic studies on nanocrystalline Co₀.₂Zn₀.₈Fe₂O₄, Mater. Res. Bull. 38(11) (2003) 1653-1660. doi:10.1016/S0025-5408(03)00175-2.

[33] K.B. Cantrell, P.G. Hunt, M. Uchimiya, J.M. Novak, K.S. Ro, Impact of pyrolysis temperature and manure source on physicochemical characteristics of biochar, Bioresour. Technol. 107 (2012) 419–428, https://doi.org/10.1016/j.biortech.2011.11.084.

[34] K. Talukdar, B.-M. Jun, Y. Yoon, Y. Kim, A. Fayyaz, C.M. Park, Novel Z-scheme Ag₃PO₄/Fe₃O₄-activated biochar photocatalyst with enhanced visible-light catalytic performance toward degradation of bisphenol A, J. Hazard. Mater. 398 (2020), 123025, https://doi.org/10.1016/j.jhazmat.2020.123025.

[35] S.E.M. Pourhosseini, O. Norouzi, H.R. Naderi, Study of micro/macro ordered porous carbon with olive-shaped structure derived from Cladophora glomerata macroalgae as efficient working electrodes of supercapacitors, Biomass Bioenergy 107 (2017) 287–298, https://doi.org/10.1016/j.biombioe.2017.10.025.

[36] H. Fu, S. Ma, P. Zhao, S. Xu, S. Zhan, Activation of peroxymonosulfate by graphitized hierarchical porous biochar and MnFe₂O₄ magnetic nanoarchitecture for organic pollutants degradation: Structure dependence and mechanism, Chem. Eng. J. 360 (2019) 157–170, https://doi.org/10.1016/j.cej.2018.11.207.

[37] Z. Zhang, L. Huang, J. Zhang, F. Wang, Y. Xie, X. Shang, Y. Gu, H. Zhao, X. Wang, In situ constructing interfacial contact MoS₂/ZnIn₂S₄ heterostructure for enhancing solar photocatalytic hydrogen evolution, Appl. Catal. B 233 (2018) 112–119, https://doi.org/10.1016/j.apcatb.2018.04.006.

[38] X. Qian, C. Wang, H. Jie, J. Lin, Sonochemical deposition of MoSₓ on ZnIn₂S₄ for photocatalytic hydrogen evolution, Mater. Lett. 247 (2019) 122–125, https://doi.org/10.1016/j.matlet.2019.03.083.

[39] Y. Liu, G. Wang, Y. Li, Z. Jin, 2D/1D Zn₀.₇Cd₀.₃S p-n heterogeneous junction enhanced with NiWO₄ for efficient photocatalytic hydrogen evolution, J. Colloid Interface Sci. 554 (2019) 113–124, https://doi.org/10.1016/j.jcis.2019.06.080.

[40] J. Cao, B. Xu, H. Lin, S. Chen, Highly improved visible light photocatalytic activity of BiPO₄ through fabricating a novel p–n heterojunction BiOI/BiPO₄ nanocomposite, Chem. Eng. J. 228 (2013) 482–488, https://doi.org/10.1016/j.cej.2013.05.008.

[41] Z. You, C. Wu, Q. Shen, Y. Yu, H. Chen, Y. Su, H. Wang, C. Wu, F. Zhang, H. Yang, A novel efficient g-C₃N₄@BiOI p–n heterojunction photocatalyst constructed through the assembly of g-C₃N₄ nanoparticles, Dalton Trans. 47 (21) (2018) 7353–7361, https://doi.org/10.1039/C8DT01322E.

[42] G. Zhao, J. Ding, F. Zhou, X. Chen, L. Wei, Q. Gao, K. Wang, Q. Zhao, Construction of a visible-light-driven magnetic dual Z-scheme BiVO₄/g-C₃N₄/NiFe₂O₄ photocatalyst for effective removal of ofloxacin: Mechanisms and degradation pathway, Chem. Eng. J. 405 (2021), https://doi.org/10.1016/j.cej.2020.126704.

[43] M. Karpuraranjith, Y. Chen, B. Wang, J. Ramkumar, D. Yang, K. Srinivas, W. Wang, W. Zhang, R. Manigandan, Hierarchical ultrathin layered MoS₂@NiFe₂O₄ nanohybrids as a bifunctional catalyst for highly efficient oxygen evolution and organic pollutant degradation, J. Colloid Interface Sci. 592 (2021) 385–396, https://doi.org/10.1016/j.jcis.2021.02.062.

[44] X.-J. Wen, C.-G. Niu, L. Zhang, C. Liang, G.-M. Zeng, An in depth mechanism insight of the degradation of multiple refractory pollutants via a novel SrTiO₃/BiOI heterojunction photocatalysts, J. Catal. 356 (2017) 283–299, https://doi.org/10.1016/j.jcat.2017.10.022.

[45] M.E. Mahmoud, M.E. Abouelanwar, S.E.M.E. Mahmoud, M. Abdel Salam, Adsorption behavior of silver quantum dots by a novel super magnetic CoFe₂O₄-biochar-polymeric nanocomposite, J. Colloid Interface Sci. 606 (2022) 1597–1608, https://doi.org/10.1016/j.jcis.2021.08.102.

[46] F. Guo, M. Li, H. Ren, X. Huang, W. Hou, C. Wang, W. Shi, C. Lu, Fabrication of p-n CuBi₂O₄/MoS₂ heterojunction with nanosheets-on-microrods structure for enhanced photocatalytic activity towards tetracycline degradation, Appl. Surf. Sci. 491 (2019) 88–94, https://doi.org/10.1016/j.apsusc.2019.06.158.

[47] D. Liu, S. Zhang, J. Wang, T. Peng, R. Li, Direct Z-Scheme 2D/2D Photocatalyst Based on Ultrathin g-C₃N₄ and WO₃ Nanosheets for Efficient Visible-Light-Driven H₂ Generation, ACS Appl. Mater. Interfaces 11 (31) (2019) 27913–27923, https://doi.org/10.1021/acsami.9b08329.

[48] Y. Zhai, B. Huang, X. Mao, M. Zheng, Effect of hot isostatic pressing on microstructure and mechanical properties of CLAM steel produced by selective laser melting, J. Nucl. Mater. 515 (2019) 111–121, https://doi.org/10.1016/j.jnucmat.2018.12.028.

[49] K. Yoon, D.-W. Cho, A. Bhatnagar, H. Song, Adsorption of As(V) and Ni(II) by Fe-Biochar composite fabricated by co-pyrolysis of orange peel and red mud, Environ. Res. 188 (2020), 109809, https://doi.org/10.1016/j.envres.2020.109809.

[50] Y. Xiao, H. Lyu, J. Tang, K. Wang, H. Sun, Effects of ball milling on the photochemistry of biochar: Enrofloxacin degradation and possible mechanisms, Chem. Eng. J. 384 (2020), https://doi.org/10.1016/j.cej.2019.123311.

[51] X. Yan, J. Qian, X. Pei, L. Zhou, R. Ma, M. Zhang, Y. Du, L. Bai, Enhanced photodegradation of doxycycline (DOX) in the sustainable NiFe₂O₄/MWCNTs/BiOI system under UV light irradiation, Environ. Res. 199 (2021), 111264, https://doi.org/10.1016/j.envres.2021.111264.

[52] J. Bolobajev, M. Trapido, A. Goi, Effect of iron ion on doxycycline photocatalytic and Fenton-based autocatalytic decomposition, Chemosphere 153 (2016) 220–226, https://doi.org/10.1016/j.chemosphere.2016.03.042.

[53] T.T.M. Hang, N.H.T. Vy, N.T. Hanh, T.-D. Pham, Facile synthesis of copper tungstate (CuWO₄) for novel photocatalytic degradation of tetracycline under visible light, Sustainable Chem. Pharm. 21 (2021), 100407.

[54] Y. Tong, S. Zhao, J. Kang, J. Shen, Z. Chen, B. Wang, L. Bi, J. Deng, Preparation of small-sized BiVO₄ particles with improved photocatalytic performance and its photocatalytic degradation of doxycycline in water, Colloids Surf. Physicochem. Eng. Aspects 620 (2021), 126412, https://doi.org/10.1016/j.colsurfa.2021.126412.

[55] X.-J. Wen, L. Qian, X.-X. Lv, J. Sun, J. Guo, Z.-H. Fei, C.-G. Niu, Photocatalytic degradation of sulfamethazine using a direct Z-Scheme AgI/Bi₄V₂O₁₁ photocatalyst: Mineralization activity, degradation pathways and promoted charge separation mechanism, J. Hazard. Mater. 385 (2020), 121508, https://doi.org/10.1016/j.jhazmat.2019.121508.

[56] L. Zhou, W. Song, Z. Chen, G. Yin, Degradation of organic pollutants in wastewater by bicarbonate-activated hydrogen peroxide with a supported cobalt catalyst, Environ. Sci. Technol. 47 (8) (2013) 3833–3839.

[57] S.J. Olusegun, N.D.S. Mohallem, Comparative adsorption mechanism of doxycycline and Congo red using synthesized kaolinite supported CoFe₂O₄ nanoparticles, Environ. Pollut. 260 (2020), 114019, https://doi.org/10.1016/j.envpol.2020.114019.

[58] K. Luo, Y. Pang, Q. Yang, D. Wang, X. Li, L. Wang, M. Lei, J. Liu, Enhanced ciprofloxacin removal by sludge-derived biochar: Effect of humic acid, Chemosphere 231 (2019) 495–501, https://doi.org/10.1016/j.chemosphere.2019.05.151.

[59] G. Fang, J. Gao, D.D. Dionysiou, C. Liu, D. Zhou, Activation of persulfate by quinones: free radical reactions and implication for the degradation of PCBs, Environ. Sci. Technol. 47 (9) (2013) 4605–4611, https://doi.org/10.1021/es400262n.

[60] D. Sun, J. Mao, L. Cheng, X. Yang, H. Li, L. Zhang, W. Zhang, Q. Zhang, P. Li, Magnetic g-C₃N₄/NiFe₂O₄ composite with enhanced activity on photocatalytic disinfection of Aspergillus flavus, Chem. Eng. J. 418 (2021), 129417.

[61] H. Che, G. Che, H. Dong, W. Hu, H. Hu, C. Liu, C. Li, Fabrication of Z-scheme Bi₃O₄Cl/g-C₃N₄ 2D/2D heterojunctions with enhanced interfacial charge separation and photocatalytic degradation various organic pollutants activity, Appl. Surf. Sci. 455 (2018) 705–716, https://doi.org/10.1016/j.apsusc.2018.06.038.

[62] H. Che, C. Liu, W. Hu, H. Hu, J. Li, J. Dou, W. Shi, C. Li, H. Dong, NGQD active sites as effective collectors of charge carriers for improving the photocatalytic performance of Z-scheme g-C₃N₄/Bi₂WO₆ heterojunctions, Catal. Sci. Technol. 8 (2) (2018) 622–631, https://doi.org/10.1039/C7CY01709J.

[63] R. Jiang, G. Lu, Z. Yan, D. Wu, R. Zhou, X. Bao, Insights into a CQD-SnNb₂O₆/BiOCl Z-scheme system for the degradation of benzocaine: Influence factors, intermediate toxicity and photocatalytic mechanism, Chem. Eng. J. 374 (2019) 79–90, https://doi.org/10.1016/j.cej.2019.05.176.

[64] S. Li, Shao, Z. Yang, S. Cheng, C. Yang, Y. Liu, X. Xia, Constructing Ti₃C₂ MXene/ZnIn₂S₄ heterostructure as a Schottky catalyst for photocatalytic environmental remediation, Green Energy Environ. (2020), https://doi.org/10.1016/j.gee.2020.09.005.

[65] F. Meng, J. Li, S.K. Cushing, M. Zhi, N. Wu, Solar hydrogen generation by nanoscale p–n junction of p-type molybdenum disulfide/n-type nitrogen-doped reduced graphene oxide, J. Am. Chem. Soc. 135 (28) (2013) 10286–10289.

[66] J. Ke, J. Liu, H. Sun, H. Zhang, X. Duan, P. Liang, X. Li, M.O. Tade, S. Liu, S. Wang, Facile assembly of Bi₂O₃/Bi₂S₃/MoS₂ n-p heterojunction with layered n-Bi₂O₃ and p-MoS₂ for enhanced photocatalytic water oxidation and pollutant degradation, Appl. Catal. B 200 (2017) 47–55, https://doi.org/10.1016/j.apcatb.2016.06.071.

[67] S.A. Rawool, M.R. Pai, A.M. Banerjee, A. Arya, R.S. Ningthoujam, R. Tewari, R. Rao, B. Chalke, P. Ayyub, A.K. Tripathi, S.R. Bharadwaj, pn Heterojunctions in NiO:TiO₂ composites with type-II band alignment assisting sunlight driven photocatalytic H₂ generation, Appl. Catal. B 221 (2018) 443–458, https://doi.org/10.1016/j.apcatb.2017.09.004.

[68] X. Li, C. Garlisi, Q. Guan, S. Anwer, K. Al-Ali, G. Palmisano, L. Zheng, A review of material aspects in developing direct Z-scheme photocatalysts, Mater. Today 47 (2021) 75–107, https://doi.org/10.1016/j.mattod.2021.02.017.